AGU PUBLICATIONS

JGR

Journal of Geophysical Research: Planets

RESEARCH ARTICLE
10.1002/2013JE004502

Key Points:
- The zonal distribution of dust forcing is key to understanding wave response
- The zonal wavenumber 1 pattern of dust forcing is the key mechanism
- High-latitude wave response is coupled to that of the tropics

Correspondence to:
S. D. Guzewich,
scott.d.guzewich@nasa.gov

Citation:
Guzewich, S. D., R. J. Wilson, T. H. McConnochie, A. D. Toigo, D. J. Banfield, and M. D. Smith (2014), Thermal tides during the 2001 Martian global-scale dust storm, *J. Geophys. Res. Planets*, *119*, 506–519, doi:10.1002/2013JE004502.

Received 14 AUG 2013
Accepted 7 FEB 2014
Accepted article online 12 FEB 2014
Published online 6 MAR 2014

Thermal tides during the 2001 Martian global-scale dust storm

Scott D. Guzewich[1], R. John Wilson[2], Timothy H. McConnochie[3], Anthony D. Toigo[4], Donald J. Banfield[5], and Michael D. Smith[1]

[1]NASA Goddard Spaceflight Center, Greenbelt, Maryland, USA, [2]Geophysical Fluid Dynamics Laboratory NOAA, Princeton, New Jersey, USA, [3]Department of Astronomy, University of Maryland, College Park, Maryland, USA, [4]Johns Hopkins University Applied Physics Laboratory, Laurel, Maryland, USA, [5]Center for Radiophysics and Space Research, Cornell University, Ithaca, New York, USA

Abstract The 2001 (Mars Year 25) global dust storm radically altered the dynamics of the Martian atmosphere. Using observations from the Thermal Emission Spectrometer onboard the Mars Global Surveyor spacecraft and MarsWRF general circulation model simulations, we examine the changes to thermal tides and planetary waves caused by the storm. We find that the extratropical diurnal migrating tide is dramatically enhanced during the storm, particularly in the southern hemisphere, reaching amplitudes of more than 20 K. The tropical diurnal migrating tide is weakened to almost undetectable levels. The diurnal Kelvin waves are also significantly weakened, particularly during the period of global expansion at $L_s = 200°–210°$. In contrast, the westward propagating diurnal wavenumber 2 tide strengthens to 4–8 K at altitudes above 30 km. The wavenumber 1 stationary wave reaches amplitudes of 10–12 K at 50°–70°N, far larger than is typically seen during this time of year. The phase of this stationary wave and the enhancement of the diurnal wavenumber 2 tide appear to be responses to the high-altitude westward propagating equatorial wavenumber 1 structure in dust mixing ratio observed during the storm in previous works. This work provides a global picture of dust storm wave dynamics that reveals the coupling between the tropics and high-latitude wave responses. We conclude that the zonal distribution of thermotidal forcing from atmospheric aerosol concentration is as important to understanding the atmospheric wave response as the total global mean aerosol optical depth.

1. Introduction

Global-scale dust storms are one of Mars' most enigmatic features. Despite the repeatability of many aspects of the Martian climate from year-to-year, global-scale dust storms do not occur annually and are greatly variable in duration and intensity [e.g., *Liu et al.*, 2003; *Smith*, 2008]. Martian global-scale dust storms have been observed to occur during the second half of the Martian year in the seasons bracketing planetary perihelion at $L_s = 251°$ when greater insolation warms the atmosphere and enhances dust lifting [*Kahn et al.*, 1992]. Typical global average visible wavelength column dust optical depths of approximately 0.3–0.5 are observed early in the Martian year when the atmosphere is less dusty. In dustier portions of the year column dust optical depth is typically twice that value [*Smith et al.*, 2001]. For the 2001 global-scale dust storm, the Thermal Emission Spectrometer (TES) onboard the Mars Global Surveyor (MGS) spacecraft retrieved infrared (9.3 μm) optical depths of 1.5–2 [*Smith et al.*, 2002], which translates to approximately twice that in visible wavelengths [*Wolff et al.*, 2006].

In 2001, or Mars Year 25 (MY25) in the calendar of *Clancy et al.* [2000], a dust storm developed unusually early in the southern hemisphere ($L_s = 184°$) just after the southern spring equinox near Hellas Basin [*Smith et al.*, 2002; *Strausberg et al.*, 2005; *Cantor*, 2007]. The storm expanded eastward as additional areas of dust lifting developed, and a thick dust cloud encircled the planet by $L_s = 197°$ [*Cantor*, 2007]. Dust reached heights of 60–80 km and took months to completely settle out of the atmosphere back to nominal levels [*Clancy et al.*, 2010].

The dust storm forced dramatic changes to atmospheric temperatures and structures. While the daytime surface temperatures cooled by 20–30 K due to decreased insolation reaching the surface, atmospheric temperatures rose by 20–40 K, depending on height [*Smith et al.*, 2002; *Smith*, 2004]. *Smith et al.* [2002] also noticed a dramatic diurnal variability in TES temperatures (20–50 K) during the storm and attributed it to enhanced thermal tides. Dust forcing of thermal tides has previously been examined in observations and general circulation models (GCMs). *Leovy and Zurek* [1979] noted significant enhancement of the migrating

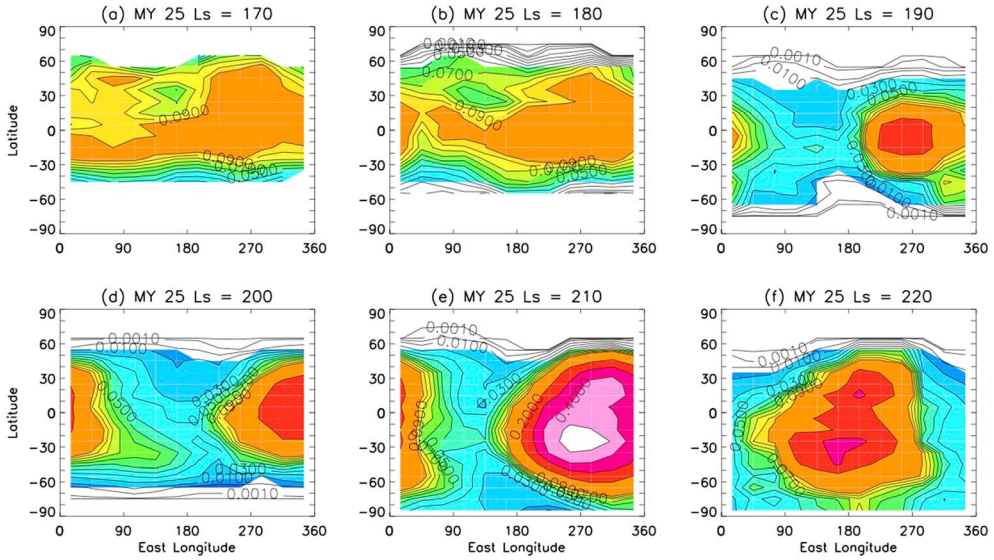

Figure 1. TES 2 P.M. dust mixing ratio ($\Delta\tau$/mb) at 60 km altitude for MY25 (a) $L_s = 170°$, (b) $L_s = 180°$, (c) $L_s = 190°$, (d) $L_s = 200°$, (e) $L_s = 210°$, and (f) $L_s = 220°$.

diurnal and semidiurnal surface pressure tides from Viking Lander pressure sensor data during both global-scale dust storms of 1977. *Haberle et al*. [1982], *Wilson and Hamilton* [1996], and *Wilson and Richardson* [2000] later modeled the 1977 global dust storms and examined the role of tides. Indeed, some studies have linked tides to the development and growth of global-scale dust storms [*Leovy and Zurek*, 1979; *Leovy*, 1981; *Basu et al*., 2006; *Wilson et al*., 2008a, 2008b] and large regional storms [*Wang et al*., 2003]. Building on those earlier studies, we find that the zonal distribution of the dust forcing is as important to the resulting wave generation as is the total dust optical depth. This zonal distribution of dust is plotted at high altitude (60 km) in Figure 1 from before the storm ($L_s = 170°$) through the initiation of storm decay ($L_s = 220°$). The slowly westward propagating dust maximum in Figure 1d–1f was first identified by *Clancy et al*. [2010], which is also described in *Guzewich et al*. [2013a] and appears to be a key player in the atmospheric wave response during the storm.

In this paper, we examine the effect of the 2001 global-scale dust storm on atmospheric thermal tides using TES observations and the MarsWRF GCM. In section 2 we describe the TES data set and the MarsWRF GCM. In section 3 we analyze and discuss the data and present our results. Finally, section 4 concludes the work.

2. Data and Model Description

2.1. TES Limb-Sounding Data Description

TES retrieved temperatures through both nadir- and limb-sounding observing modes during its mission. This study uses primarily limb-sounding data, but nadir-derived data are incorporated into the retrieved temperature profiles. Indeed, below 80 Pa (approximately 22 km altitude), the data are 100% derived from nadir-viewing observation. The limb-viewing observations are then phased into the nadir observations above 80 Pa and above 10 Pa, all data are derived from limb observations. The primary difference to the TES temperature retrievals described by *Smith et al*. [2001] is that errors have been significantly reduced through accurate instrument background measurements and noise covariance matrices [*McConnochie and Smith*, 2011] (for additional details, see *Guzewich et al*. [2013a, Appendix 1]). The temperature retrieval algorithm is performed first and the aerosol opacities retrieved second. At very high opacities, as was seen during the height of the 2001 global-scale dust storm, this may create larger temperature errors (the errors could be as large as 5–20 K) in the nadir-viewing geometry in the lowest 1–1.5 scale heights of the atmosphere (with errors increasing toward the surface). We have performed sensitivity tests of this scenario and find that above 1.5 scale heights, the temperature errors are comparable to the low-opacity errors: 1–3 K, which is 2% or less of typical temperatures. Altitudes below 1.5 scale heights above the surface are not plotted in the figures. The limb-derived temperatures may also be biased near 4 scale heights (the lowest altitude where the temperature profile is almost completely derived from limb-viewing observations) through dust absorption

Table 1. Waves Discussed

Field Type	s	σ	Comments
		$m=0$	
Average	0	0	Zonal Mean Temperature
	2	2	
Difference	1	1	Migrating Diurnal Tide
	3	3	
		$m=1$	
Average	1	0	Stationary Wave 1
	1	2	
Difference	0	1	Diurnal Zonally Symmetric Tide
	2	1	Diurnal Westward Wave 2
		$m=2$	
Average	2	0	Stationary Wave 2
	0	2	
Difference	1	−1	Diurnal Kelvin Wave 1
	3	1	Diurnal Westward Wave 3
		$m=3$	
Average	3	0	Stationary Wave 3
	1	−2	
Difference	2	−1	Diurnal Kelvin Wave 2
	4	1	Diurnal Westward Wave 4

and scattering from the surface. However, at 5 scale heights and above, the dust opacity is too low to bias the temperature retrieval. The smooth continuity in temperatures and wave amplitudes between the two altitude regions of highest reliability (1.5–4 and above 5 scale heights) and corroboration from the general circulation model gives us high confidence in our results and interpretations.

Data were binned by 10° latitude, 30° longitude, and 10° of solar longitude resulting in approximately 50 temperature profiles averaged together to produce one bin value. Because MGS flew a Sun-synchronous orbit, observations were constrained to be at approximately 2:00 A.M. and 2:00 P.M. local solar time. Our binning divided temperatures into either "morning" or "afternoon" (T_{2am} and T_{2pm}). At very high latitudes, the local time of the observations deviates somewhat from the nominal 2:00 A.M. and 2:00 P.M. times. This may complicate our analysis at those latitudes, but at middle and low latitudes where our analysis is focused, the typical deviations from the nominal local times are less than 1 h and have negligible effect on this analysis.

In our analysis, we assume an atmospheric wave has functional dependence on longitude (λ), pressure (p), latitude (ϕ), and time (t). In a Sun-synchronous frame of reference, local time is fixed. We neglect the pressure dependence to produce the following wave equation:

$$T(\lambda, t_{LST}) = \Sigma A_{s,\sigma} \cos[(s-\sigma)\lambda + \sigma t_{LST} + \delta] \quad (1)$$

where A is the amplitude of a wave with wavenumber s and frequency per sol σ, t_{LST} is local solar time, and δ is an arbitrary phase. Positive (negative) σ denotes westward (eastward) wave propagation. Analysis of the tides proceeded as many previous studies [*Banfield et al.*, 2003; *Lee et al.*, 2009; *Guzewich et al.*, 2012] by creating "average" and "difference" temperatures of the morning and afternoon observations.

$$T_{avg} = (T_{2pm} + T_{2am})/2 \quad (2)$$

$$T_{dif} = (T_{2pm} - T_{2am})/2 \quad (3)$$

Based on the offset of π radians between the 2:00 P.M. and 2:00 A.M. local solar times, equations (1)–(3) can be combined and solved for T_{avg} and T_{dif}, the solutions of which differ by only a factor of $(-1)^{\sigma}$. Thus, only terms with even (odd) σ appear in the T_{avg} (T_{dif}) fields (see *Guzewich et al.* [2012] for additional details). For example, stationary waves ($\sigma=0$) and semidiurnal tides ($\sigma=2$) appear in the T_{avg} fields, while diurnal tides ($\sigma=1$) appear in the T_{dif} fields. We then apply a Fourier transform to the T-average and T-difference temperature fields. The Sun-synchronous viewpoint aliases tides (and stationary planetary waves) into satellite-relative wavenumber fields (denoted by m henceforth). A wave observed in wavenumber m field can be any combination of waves where $m=|s-\sigma|$ [*Forbes and Hagan*, 2000; *Wilson*, 2000; *Lee et al.*, 2009]. Table 1 identifies the waves discussed in this work and which wavenumber m field they manifest. In part, we attribute temperature amplitudes in a given T_{avg} or T_{dif} field to a given wave (tide or stationary wave) by the difference in phase progression direction in height (eastward or westward) and the rate at which the phase changes with height (slowly for a long wavelength, quickly for a short).

2.2. TES T_{15} Data Description

In an effort to expand and corroborate the limb-sounding data set described in section 2.1, we utilize TES 15 μm brightness temperatures obtained through nadir-viewing observations, referred to henceforth as T_{15}. These data provide a depth-weighted view of atmospheric temperature, approximately representative of the 50 Pa (25 km) level in the atmosphere [*Wilson and Richardson*, 2000]. They have longitudinal and temporal

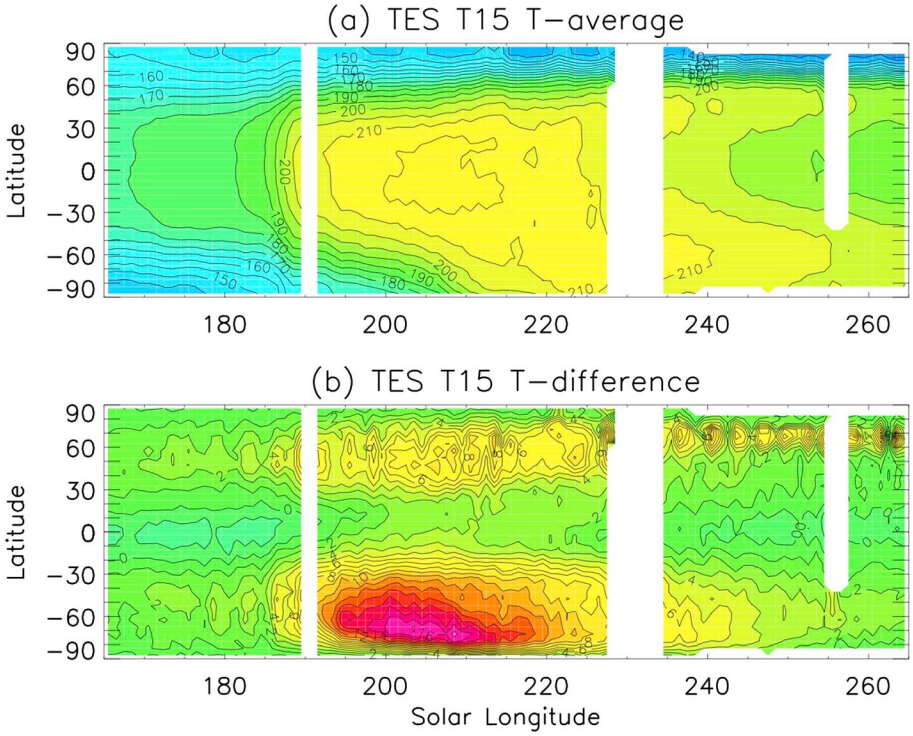

Figure 2. (a) Zonally averaged TES T_{15} *T*-average temperatures and (b) *T*-difference temperatures during MY25.

resolution of 3° and 0.5°, respectively, both of which are much higher than the limb-sounding data set. Analysis of the T_{15} proceeded exactly as that of the limb-sounding data with calculating average and difference temperatures and then taking a Fourier transform of those. The depth-weighting will provide an underestimate of amplitude of waves with short vertical wavelengths (e.g., the westward propagating diurnal nonmigrating tides) while accurately representing those with longer vertical wavelengths (e.g., the diurnal Kelvin waves).

2.3. MarsWRF Description

MarsWRF is the Mars-specific implementation of PlanetWRF, a generalized planetary atmosphere general circulation model developed from the terrestrial Weather Research and Forecasting (WRF) model [*Richardson et al*., 2007; *Toigo et al*., 2012]. *Guzewich et al*. [2013b] describes how the dust distribution of MarsWRF was modified to utilize a dust climatology derived from the TES limb-geometry observations described by *Guzewich et al*. [2013a]. For this work, we utilize a 3 Mars year simulation that "replays" Mars Years 24–27 and includes the 2001 global-scale dust storm. This is simulation S5 in the nomenclature of *Guzewich et al*. [2013b], and we will refer to it as the "dust storm simulation." We use a "standard" MarsWRF simulation (described as simulation S1 by *Guzewich et al*. [2013b] and the "standard resolution" simulation by *Toigo et al*. [2012]) to serve as a control to compare against. The control simulation uses the "MGS scenario" Mars Climate Database dust prescription described by *Montmessin et al*. [2004], which uses a modified Conrath-ν vertical dust profile [*Conrath*, 1975; *Montmessin et al*., 2004] and an analytic function describing the latitudinally and seasonally varying dust opacity typical of a year without a global-scale dust storm. Additionally, a more generic "dust storm" simulation is conducted where the vertical dust prescription of the "MGS Scenario" in the Mars Climate Database is used, but the visible band optical depth at a reference pressure of 610 Pa is globally set equal to 2.

3. Analysis and Discussion

3.1. Migrating Diurnal Tide

The migrating diurnal tide is the westward propagating Sun-synchronous wavenumber 1 response to solar heating that occurs in planetary atmospheres [*Chapman and Lindzen*, 1970]. As with Earth, the gravest Hough

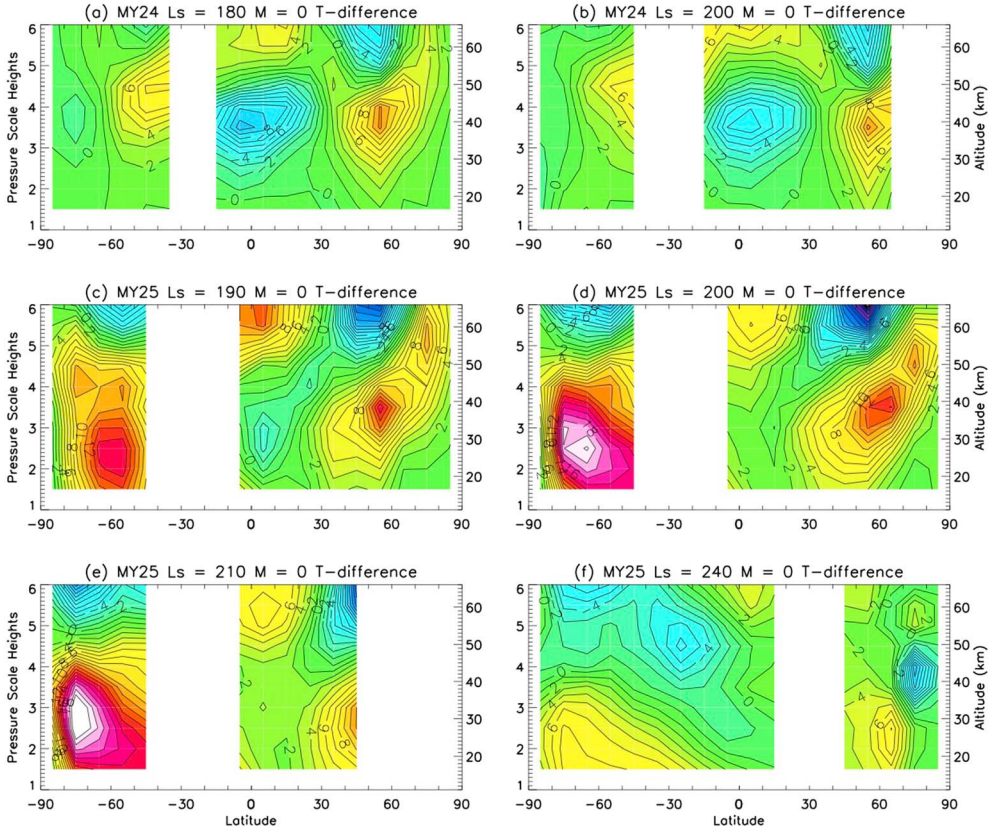

Figure 3. Amplitude of the observed limb-sounding TES $m = 0$ *T*-difference field for (a) MY24 $L_s = 180°$, (b) MY24 $L_s = 200°$, (c) MY25 $L_s = 190°$, (d) MY25 $L_s = 200°$, (e) MY25 $L_s = 210°$, and (f) MY25 $L_s = 240°$. This represents the migrating diurnal tide.

mode of the tide is equatorially trapped in the low latitudes on Mars (due to the apparent singularity near 30° where the Coriolis frequency equals the diurnal frequency). At higher latitudes, vertically trapped modes dominate. Previous modeling studies [e.g., *Wilson and Richardson*, 2000] have indicated that while the gravest Hough mode of the migrating diurnal tide is weakened by significant dust loading, the vertically trapped extratropical modes are strongly forced by atmospheric dust.

In Figures 2a and 2b, we show the TES T_{15} *T*-average and *T*-difference fields, respectively. The *T*-average temperature represents the zonal mean temperature and shows the rapid 20 K temperature increase in the lower atmosphere associated with the storm. The *T*-difference temperature demonstrates the intense thermotidal forcing associated with the storm from $L_s = 190°$ and $L_s = 220°$ when optical depths were largest, causing the very large amplitudes in the middle latitudes of both hemispheres. Due to the nature of the T_{15} observations, the tropical migrating diurnal tide is not well represented (even prior to the storm), while the amplitudes of the vertically trapped extratropical modes are representative.

However, as seen in the TES limb-sounding observations, the tropical migrating diurnal tide was weakened during the storm. In Figures 3a and 3b, we illustrate the $m = 0$ *T*-difference field of the TES limb-sounding observations at $L_s = 180°$ and $L_s = 200°$, respectively, for MY24. This provides a view of the "expected" nondust storm pattern to the migrating diurnal tide with a look of alternating minima and maxima in the vertical with amplitudes of approximately 8 K. A similar pattern is evident in MY25 at $L_s = 180°$, but the data coverage is significantly less than in MY24, and hence is not shown. This pattern is most apparent during the equinox seasons when the tropical migrating diurnal tide response is strongest. Similar structures have been observed with TES by *Banfield et al.* [2003] and Mars Climate Sounder by *Lee et al.* [2009] and *Guzewich et al.* [2012]. Immediately following the onset of the storm at $L_s = 190°$ in MY25 (Figure 3c), the extratropical tide becomes significantly stronger with amplitudes of 15 K in the southern hemisphere at 50°–60°S and 20–30 km and 10–12 K at a comparable location in the northern hemisphere. The equatorial structure is still present but

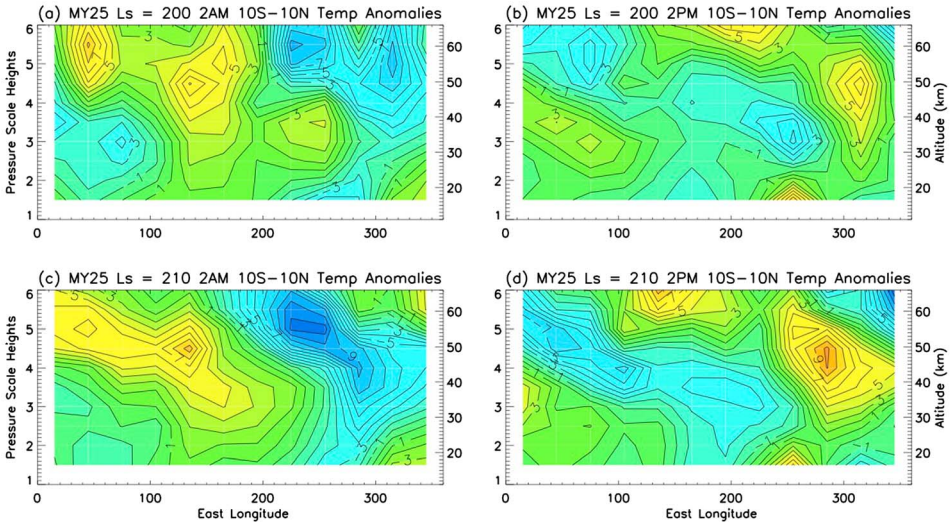

Figure 4. TES observed limb-sounding equatorial (10°S–10°N) temperatures anomalies (temperature minus zonal mean temperature) for MY25: (a) 2 A.M. $L_s = 200°$, (b) 2 P.M. $L_s = 200°$, (c) 2 A.M. $L_s = 210°$, and (d) 2 P.M. $L_s = 210°$.

has been weakened relative to $L_s = 180°$. As the storm became global near $L_s = 200°$, the observations indicate the vertically propagating tropical mode becomes completely suppressed (Figure 3d) and the extratropical vertically trapped modes are dominant through $L_s = 290°$. The amplitude of the extratropical tide peaks at $L_s = 200°$–$210°$ (Figures 3d and 3e) at 20–22 K in the southern hemisphere when globally averaged opacity was greatest, while the northern hemisphere (within latitudes of retrieved data) amplitude remains steady near 10–12 K. The observed southern hemisphere extratropical tide amplitude decreases soon after the storm reached maximum optical depth and dust lifting ceased (Figures 2b and 3f). Still, the extratropical tide amplitude remains anomalously high relative to nondust storm conditions, even for the dusty near-perihelion season, through northern fall and winter (compare Figure 3f with *Guzewich et al.* [2012, Figure 4c]). The vertically propagating tropical tide mode does not clearly reemerge until after $L_s = 270°$.

3.2. Nonmigrating Tides

Nonmigrating tides are those that are not Sun-synchronous, can propagate eastward or westward (depending on the particular tide), and are forced by a suite of atmospheric processes including interactions of the migrating tides and topography [*Chapman and Lindzen*, 1970], tide-Rossby wave interactions [*Moudden and Forbes*, 2011a, 2011b], and others.

Among the nonmigrating tides on Mars, the diurnal Kelvin wave 1 (DK1) has been the most thoroughly studied in the literature. *Zurek and Leovy* [1981], *Wilson and Hamilton* [1996], and *Bridger and Murphy* [1998] examined the behavior of DK1's surface pressure signal in Viking Lander data during the 1977 global dust storms, and they found that the DK1 pressure tide was enhanced during the storm, leading to destructive interference between it and the westward propagating migrating diurnal tide. *Martinez-Alvarado et al.* [2009] and *Montabone et al.* [2008] (using a Mars data assimilation data set based on TES observations [*Montabone et al.*, 2006]) speculated that a shift in phase of combined DK1 and migrating diurnal tide surface pressure signals, associated with dust heating near Hellas Basin from the onset of the 2001 storm, enhanced dust lifting in the Tharsis region and allowed the storm to strengthen. Still, the temperature amplitude of DK1 is expected to remain relatively invariant to zonally uniform aerosol loading due to a balancing between a near-resonant response in the cool dust-free atmosphere and stronger migrating tide forcing during enhanced aerosol loading [*Zurek*, 1988; *Wilson and Hamilton*, 1996; *Guzewich et al.*, 2013b].

DK1 has been identified in many observations of the Martian atmosphere [e.g., *Banfield et al.*, 2003; *Wilson*, 2000, 2002; *Hinson et al.*, 2001; *Withers et al.*, 2011; *Guzewich et al.*, 2012] and exhibits amplitudes of 1–4 K with a very long vertical wavelength resulting in no-phase progression with height (i.e., a barotropic structure). Due to the aliasing associated with a Sun-synchronous orbit, DK1 appears in the $m = 2$ T-difference field and will appear as a wavenumber 2 structure in longitude in the T_{2am} and T_{2pm} fields. This wavenumber 2

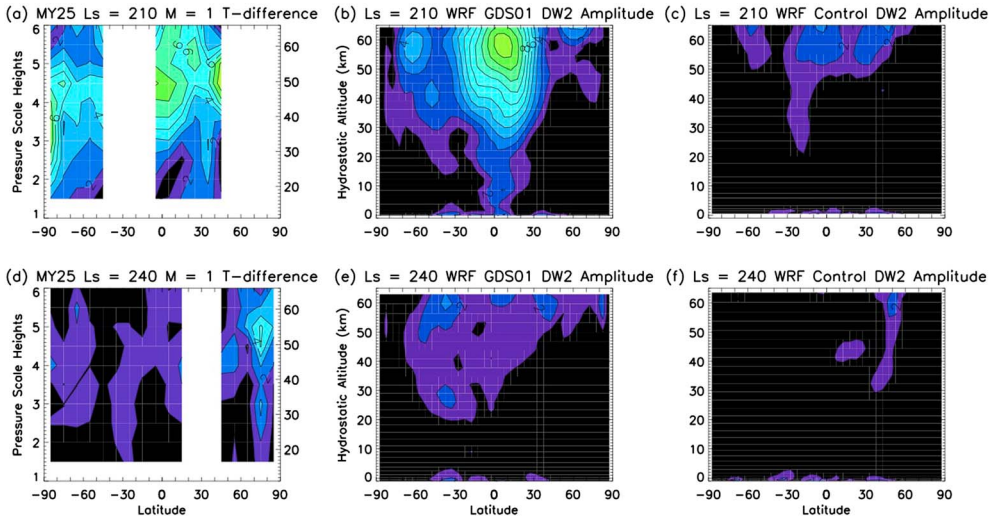

Figure 5. (a) MY25 $L_s = 210°$ amplitude of the observed limb-sounding TES $m = 1$ *T*-difference field, (b) diurnal westward wavenumber 2 tide amplitude from the MarsWRF global dust storm simulation, and (c) diurnal westward wavenumber 2 tide amplitude from the MarsWRF control simulation. (d–f) The same fields for MY25 $L_s = 240°$.

structure is clearly apparent in the TES temperature fields in nearly all seasons with a sign change between 2 A.M. and 2 P.M. (i.e., out of phase with each other, indicating a diurnal wave). During the 2001 global-scale dust storm, the dominance of DK1 over the nonmigrating tide temperature structure broke down. At $L_s = 190°$ in the TES observations, the equatorial (10°S–10°N) T_{2am} and T_{2pm} fields begin to lose the barotropic wavenumber 2 structure previously present and develop a wavenumber 1 structure with a strong westward phase tilt with height (not shown). The westward propagation in phase is indicated by the increasingly westward location of temperature maxima or minima with increasing altitude. *Lewis and Barker* [2005] and *Wilson et al.* [2008a, 2008b] found that the amplitude of DK1 in the surface pressure signal dropped during the 2001 global-scale dust storm (well after storm onset) in a Mars data assimilation data set described in *Montabone et al.* [2006]. Figure 4 shows the limb-sounding observed 2 A.M. and 2 P.M. temperatures (with the zonal mean temperature subtracted) for $L_s = 200°–210°$ (averaged between 10°S and 10°N) that most clearly shows this westward propagating wavenumber 1 field, particularly above 30 km altitude. We interpret this as a diurnal westward propagating wavenumber 2 nonmigrating tide (DW2), which appears as a wavenumber 1 structure in a Sun-synchronous (fixed local time) reference and contributes to the $m = 1$ *T*-difference field.

The gravest Hough mode of DW2 has a relatively short theoretical vertical wavelength of 31.5 km and is equatorially confined to roughly 25° in each hemisphere (calculated using tidal theory as described in *Chapman and Lindzen* [1970]). Higher-order modes contribute to this tide in the extratropics. The $m = 1$ *T*-difference field shows the strong amplification of this tide with 4–8 K amplitudes at higher altitudes (above 30 km) at $L_s = 200°–210°$ (Figure 5a). Also contributing to the $m = 1$ *T*-difference field is the zonally symmetric diurnal tide (see Table 1). The zonally symmetric tide has no phase progression with height, in contrast to the clear westward phase progression of the T_{2am} and T_{2pm} fields. The MarsWRF dust storm simulation does show an amplification of the zonally symmetric tide during the storm (increasing from 1 K to 2–3 K); however, the amplitude is less than half the amplitude of the simulated DW2 during most of $L_s = 200°–240°$ at low and middle latitudes (Figures 6a and 6d). Figure 6a shows the MarsWRF simulation of the 2001 global-scale dust storm mimicking this amplification with a rapid increase in DW2 amplitude at an approximate height of 45 km from around 1 K to more than 6 K immediately following global expansion of the dust storm at $L_s = 205°$, with a smaller but analogous increase in amplitude during the first phase of dust lifting near $L_s = 180°$. Using a Fourier analysis of the MarsWRF temperature fields in longitude and time, the direct DW2 tidal amplitude is seen in Figures 5b, 5c, and 6a–6c, without the aliasing implicit in the TES *T*-difference and *T*-average fields. The MarsWRF dust storm simulation clearly shows the strong amplification of DW2 during the storm (Figure 5b), exceeding 10 K at high altitudes, compared to the very weak amplitudes seen in the control simulation (Figure 5c). Equatorial DW2 amplitudes in the control simulation remain less than 2 K for the entire simulation (Figures 5c and 6b). By $L_s = 230–240°$ the amplitude of the observed $m = 1$ *T*-difference field

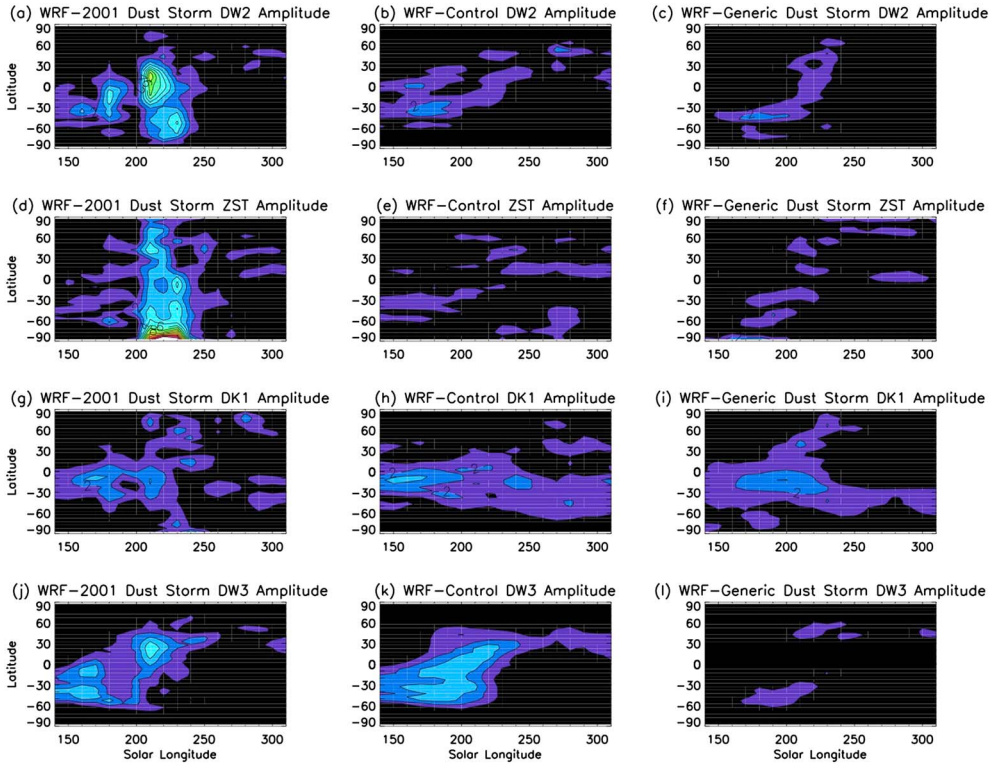

Figure 6. Simulated tidal amplitude at approximately 45 km altitude for the (a, d, g, j) WRF global dust storm simulation, (b, e, h, k) control simulation, and (c, f, i, l) generic dust storm simulation for four nonmigrating tides. Tides plotted are the (Figures 6a–6c) diurnal westward wavenumber 2 tide, (Figures 6d–6f) zonally symmetric tide, (Figures 6g–6i) diurnal wavenumber 1 Kelvin wave, and (Figures 6j–6l) diurnal westward wavenumber 3 tide.

decreases by more than 50% near the equator (Figure 5d), and this pattern is duplicated in the MarsWRF dust storm simulation (Figures 5e and 6a). The control simulation continues to show amplitudes that are weaker still (Figures 5f and 6b).

The amplification of DW2 is also seen in T_{15} observations (Figure 7a), although to a lesser degree due to the depth weighting of the T_{15} observations smoothing the amplitudes of this tide. Still, a clear enhancement and near 180° phase shift is seen associated with the initial dust lifting near Hellas around $L_s = 185°$. Amplitudes remain higher through $L_s = 220°$ before a rapid weakening thereafter. The nearly 180° phase shifts indicated in DW2 in Figure 7a between $L_s = 185°$–$220°$ are represented in the MarsWRF dust storm simulation as well.

The reason for this intense amplification of DW2 is the longitudinal structure present in the dust mixing ratios (and hence the thermotidal heating) during the storm. *Clancy et al.* [2010] and *Guzewich et al.* [2013a] both describe the large wavenumber 1 pattern in dust mixing ratio seen at high altitudes (near 60 km) during the storm, and it is reproduced in Figures 1c–1f. The response to this intense wavenumber 1 forcing modulation is the strengthened DW2. To test this, we conducted a "generic" dust storm simulation without the vertical and horizontal structure in dust mixing ratio that TES observed with global optical depths set to 2 at a reference pressure of 610 Pa. Thus, this simulation has none of the zonal structure in dust mixing ratio exhibited in the 2001 global-scale dust storm while possessing comparable total atmospheric dust loading. Indeed, with comparably high global dust opacity but without the wavenumber 1 pattern in tropical high-altitude dust mixing ratio, the DW2 tide is weak and very similar in amplitude to that seen in the control simulation (Figure 6c). The generic dust storm simulation suppresses most of the nonmigrating tides (Figures 6c, 6f, and 6l) except for DK1 (Figure 6i) which tidal theory suggests should be relatively invariant with changing atmospheric dust loadings [e.g., *Guzewich et al.*, 2013b] and is indeed relatively unchanged in the generic dust storm scenario.

Not only does DW2 dominate the observed nonmigrating tide field during the $L_s = 200°$–$210°$ period (e.g., Figure 3), but DK1 seems to weaken, confirming the result of *Lewis and Barker* [2005] and *Wilson et al.* [2008a, 2008b] in surface pressure analysis. In the MarsWRF control simulation, the mean equatorial (10°S–10°N)

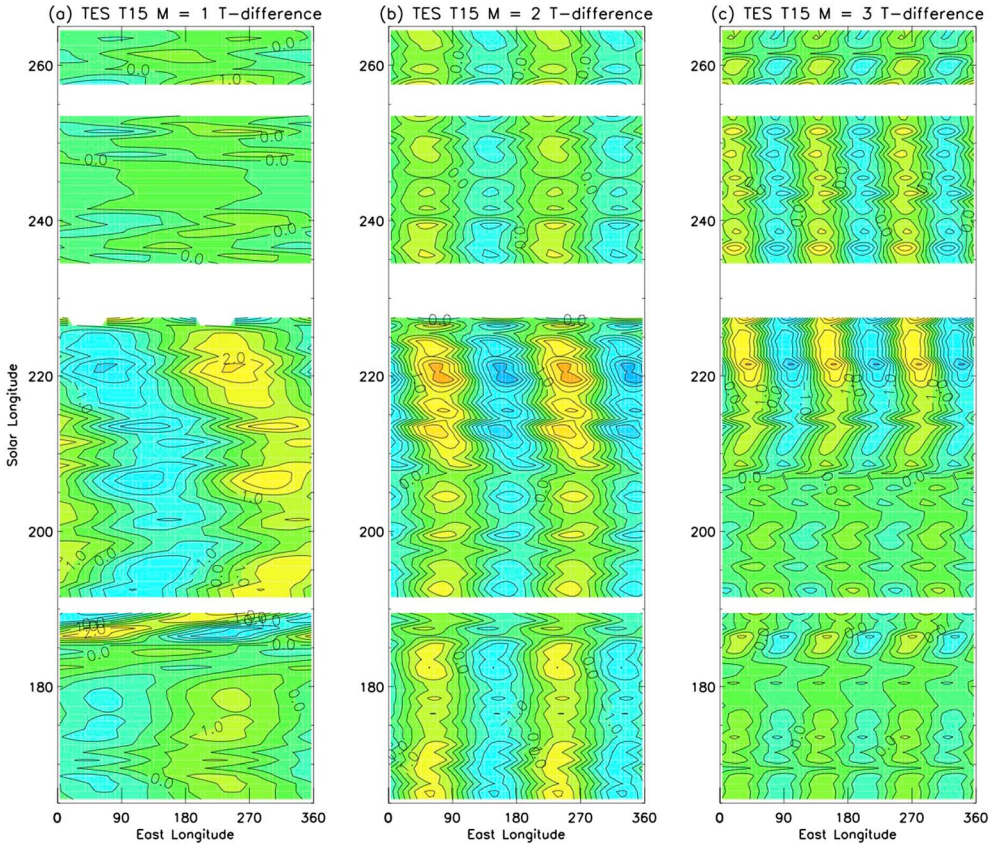

Figure 7. Fourier fits in longitude over time in MY25 of the 10°S–10°N TES T_{15} *T*-difference temperatures for (a) wavenumber 1, (b) wavenumber 2, and (c) wavenumber 3.

amplitude is 1.5–2 K throughout the year, with the minimum occurring during the dustier near-perihelion portion of the year (Figure 6h). In the dust storm simulation, the amplitude is approximately 0.5 K weaker during and after the global dust storm (Figure 6g). This change is also reflected in the observed $m = 2$ *T*-difference field (Figure 8) where the equatorial amplitude decreases from >4 K before the storm and in nondust storm years (Figures 8a and 8b) to 1–2 K in MY25 $L_s = 200°$–$210°$ (Figures 8d and 8e) before increasing modestly near $L_s = 220°$ (Figure 8f). To confirm this weakening, we examined the TES T_{15} observations. Figure 7b shows the $m = 2$ component of the *T*-difference temperature, which is representative of DK1 and confirms this slight weakening (and phase shift) after initial dust lifting at $L_s = 185°$. DK1 remains relatively weak through $L_s = 210°$ when it begins to strengthen in the T_{15} observations. The strengthening after $L_s = 210°$ seen in both types of TES observations makes sense in light of the state of the storm at that point, when dust lifting was occurring in both hemispheres (near Solis Planum and Hellas Basin) providing a $s = 2$ component to the thermotidal forcing. DK1 is forced by the interaction of the migrating diurnal tide with the $s = 2$ component of the topography and thus an additional $s = 2$ component to the thermotidal forcing should enhance DK1 at this phase of the storm. As the dust lifting ceased after $L_s = 220°$, this additional forcing was removed and both the T_{15} and limb-sounding observations show DK1 weakening yet again.

In addition to DK1, the westward diurnal wave 3 nonmigrating tide (DW3) also contributes to the $m = 2$ *T*-difference field, and both MarsWRF simulations produce comparable amplitudes between DW3 and DK1 (Figures 6g, 6h, 6j, and 6k). DW3 has a much shorter vertical wavelength than DK1. Profiles of the phase of the observed $m = 2$ *T*-difference field (not shown) are a means to distinguish the influence of these two tides on this aliased satellite-relative field. Prior to the storm, the phase of the observed $m = 2$ *T*-difference field is roughly constant with height near the equator, indicative of the dominance of DK1 over this field. However, at $L_s = 210°$ there is clear westward propagation of phase with height from 40 to 60 km. By $L_s = 240°$, the observed phase looks similar to the prestorm phase diagrams, with roughly constant phase with height in the equatorial latitudes. We interpret this as likely brief amplification of DW3 near $L_s = 200°$–$220°$ (replicated in the

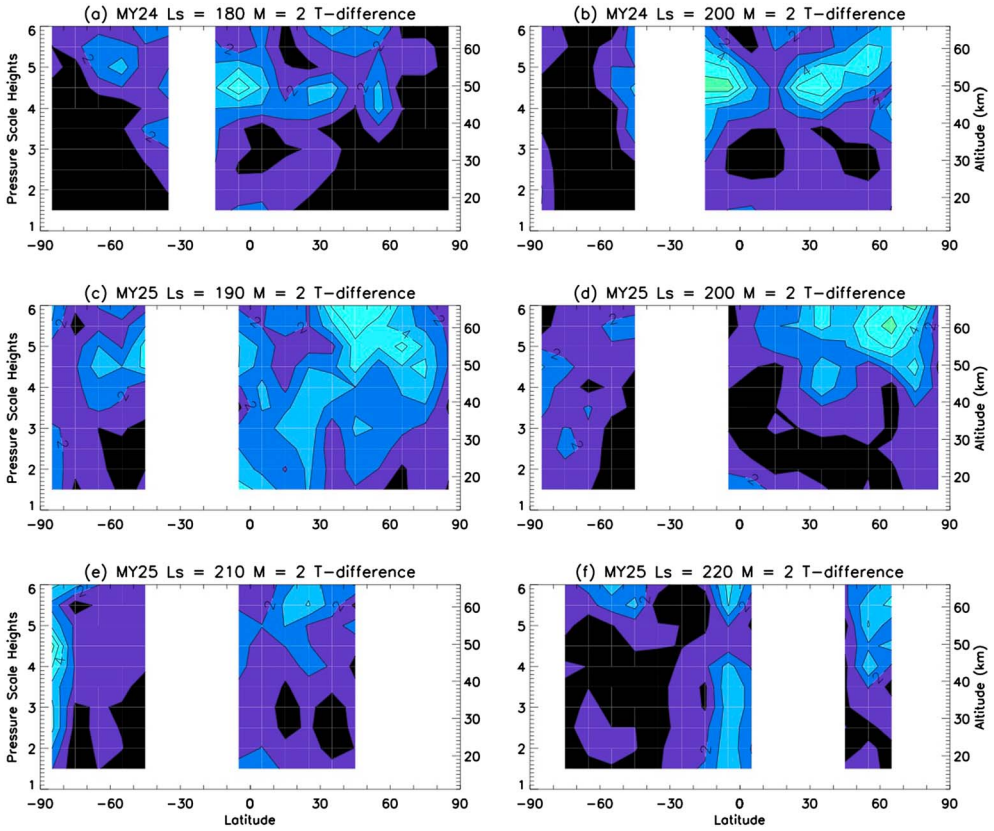

Figure 8. Amplitude of the observed limb-sounding TES $m = 2$ *T*-difference field for (a) MY24 $L_s = 180°$, (b) MY24 $L_s = 200°$, (c) MY25 $L_s = 190°$, (d) MY25 $L_s = 200°$, (e) MY25 $L_s = 210°$, and (f) MY25 $L_s = 220°$. This represents DK1.

MarsWRF simulation in Figure 6j) to dominate the observed $m = 2$ *T*-difference field before it weakens, and the two tides are roughly comparable in amplitude for the remainder of the storm until $L_s = 240°$. However, the observed amplification of DW3 may simply be part of its seasonal cycle (as seen in the control MarsWRF simulations, Figure 6k), which was only apparent because of the weakening of DK1. Given the strong wavenumber 1 pattern to the thermotidal forcing (as exhibited in the pattern of high-altitude dust mixing ratio), we would not expect DW3 to be more strongly forced than is typical at this time of year.

The observed $m = 3$ *T*-difference field, representing a combination of the wavenumber 2 diurnal Kelvin wave (DK2) and westward diurnal wavenumber 4 tide (DW4) (see Table 1), is similarly weakened during the storm. This is indicated in the T_{15} observations in Figure 7c. Equatorial amplitudes of 4–5 K are present in the limb-sounding observations at $L_s = 180°$, which weaken to 1–2 K by $L_s = 200°$. The amplitudes increase again after $L_s = 210°$ and return to 4–5 K by $L_s = 250°$. The MarsWRF dust storm simulation portrays a dramatic weakening of both the DK2 and DW4 amplitudes during the storm relative to the control simulation (by more than 50%, not shown). This further confirms the trend of weakening nonmigrating tides during the storm, with the exception of DW2 and possibly DW3.

3.3. Stationary Waves

Stationary planetary waves are forced by zonal wind flow over topography. On Mars, the dramatic (high-amplitude) topography forces wavenumber 1 and 2 ($s = 1$ and $s = 2$, respectively) stationary waves in both hemispheres, with the former dominating the southern hemisphere and latter the northern hemisphere due to the predominant topography in each [*Banfield et al.*, 2003]. The observed $s = 1$ stationary wave (represented in the $m = 1$ *T*-average field) is significantly amplified in the northern hemisphere during the storm. At $L_s = 170°$, very weak amplitudes are present in the $m = 1$ *T*-average field, consistent with the MarsWRF dust storm and control simulations. As northern hemisphere fall begins, the $s = 1$ stationary wave is expected to strengthen in the north, but the development of the global-scale dust storm enhances this

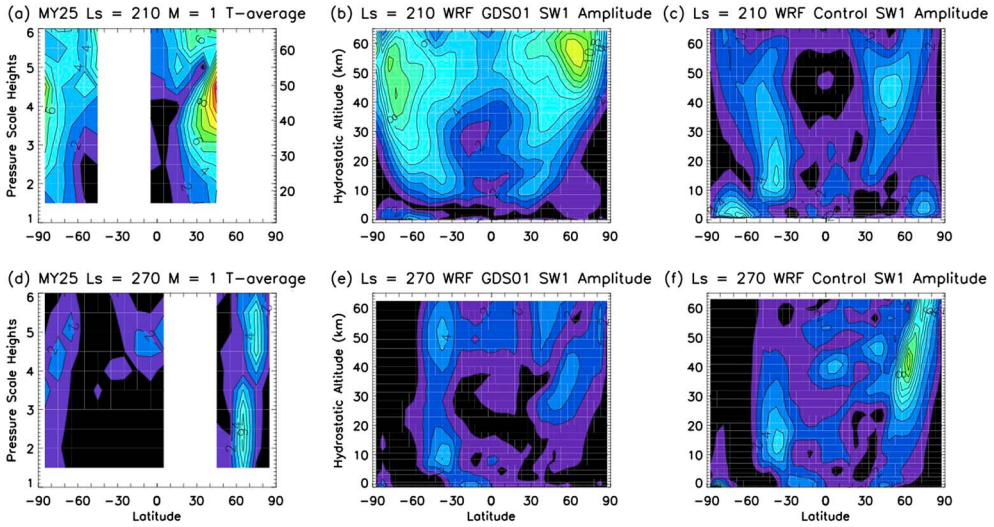

Figure 9. (a) MY25 $L_s = 210°$ amplitude of the TES limb-sounding observed $m = 1$ *T*-average field, (b) stationary wave 1 amplitude from the MarsWRF global dust storm simulation, and (c) stationary wave 1 amplitude from the MarsWRF control simulation. (d–f) The same fields for MY25 $L_s = 270°$.

process. By $L_s = 180°$, a 6–7 K amplitude maximum is observed near 30–50 km altitude at 50°–70°N (not shown). This wave response continues to strengthen through $L_s = 210°$–$220°$, when amplitudes reach 11–13 K (within regions of retrieved data, Figure 9a). A similar response is seen in the MarsWRF dust storm simulation, although in the GCM the amplitude max occurs at higher altitudes (50–70 km, Figure 9b). By contrast, the control MarsWRF simulation shows much weaker amplitudes (Figure 9c). Interestingly, the $s = 1$ stationary wave response is favored, while the $s = 2$ stationary wave remains weak. This is in contrast to the usual stationary wave behavior in the northern hemisphere, where the $s = 2$ stationary wave is favored due to the predominantly $s = 2$ topography of the northern lowlands [*Banfield et al*., 2003; *Guzewich et al*., 2012]. The MarsWRF dust storm simulation also produces a strong $s = 2$ stationary wave response in the tropics, but this is not observed in the TES data.

The $s = 1$ stationary wave in the northern hemisphere may be a response to a westward propagating equatorial wavenumber 1 structure that appears during the 2001 global-scale dust storm as indicated by TES limb-sounding observations of dust mixing ratio (Figures 1c–1f) [*Clancy et al*., 2010; *Guzewich et al*., 2013a]. Interestingly, the observed phase of the $s = 1$ stationary wave near the amplitude maximum in the northern hemisphere is not constant during the storm (as would be expected without the storm) [e.g., *Guzewich et al*., 2012] but follows the high-altitude dust mixing ratio pattern with time before "normalizing" to the expected value of ~30–50°E after $L_s = 270°$. Due to this steady change in phase, we will refer to this wave as "quasi-stationary." This may in fact also be an indication of a slow-period traveling wave, similar to that described by *Wilson et al*. [2002] and *Banfield et al*. [2004], although eastward traveling waves would normally be expected in this season. This change in phase is demonstrated in Figure 10, where the 60 km altitude TES dust mixing ratios from Figure 1 are plotted for $L_s = 190$–$210°$. Figure 10 (solid black line) indicates the phase of the

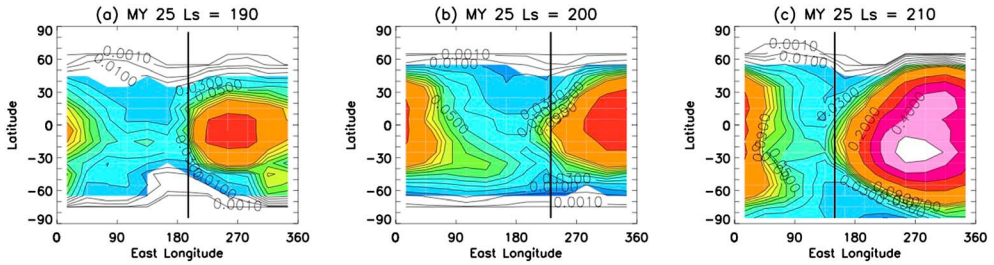

Figure 10. TES 2 P.M. dust mixing ratio ($\Delta\tau$/mb) at 60 km altitude for MY25 (a) $L_s = 190°$, (b) $L_s = 200°$, and (c) $L_s = 210°$. Solid black line indicates the phase (in east longitude) of the maximum amplitude of the northern hemisphere wavenumber 1 stationary wave.

maximum amplitude of the northern hemisphere $s = 1$ quasi-stationary wave at each time step. During the $L_s = 190°–220°$ period, when the equatorial wavenumber 1 structure is most obvious in the dust mixing ratio plots at high altitude (50–60 km), the phase of the northern hemisphere $s = 1$ quasi-stationary wave (represented by the $m = 1$ *T*-average field) directly corresponds to the leading (western) edge of the higher dust mixing ratios and the eastern edge of the "dust-free corridor" described by *Clancy et al*. [2010]. *Wilson et al*. [2002] suggested that tropical inertial instability maintains an eastward propagating slow $s = 1$ traveling wave following the results of *Salby and Callaghan* [2001]. Although we cannot directly test for observed tropical inertial instability in the TES data, we can do so in the MarsWRF simulations. We find a large region of inertial instability (as manifested by negative absolute vorticity in the northern hemisphere) is present in the low latitudes (0–10°N) of the dust storm simulation during the $L_s = 190°–220°$ period that is absent in the control simulations (not shown). This suggests that during the period of highest dust opacity, tropical inertial instabilities did at least maintain the quasi-stationary or slow-traveling wave seen in the northern hemisphere during the storm.

Even after the storm decayed at $L_s = 270°$, the observed TES $s = 1$ quasi-stationary wave amplitude remains relatively weak (Figure 9d) which is generally reflected in the MarsWRF dust storm simulation (Figure 9e) relative to a "normal" year seen in the control simulation (Figure 9f) with much larger wave amplitude.

4. Conclusions

The 2001 (MY25) global-scale dust storm initiated dramatic changes to the wave structure of the Martian atmosphere. Using temperature retrievals and brightness temperatures from TES observations and supporting information from a MarsWRF general circulation model simulation of the dust storm, we have identified several significant and unique changes to the thermal tides and stationary waves forced by the dust storm.

As expected from previous studies [e.g., *Wilson and Hamilton*, 1996], the vertically trapped extratropical modes (in the summer hemisphere) of the diurnal migrating tide are strongly forced by the high-column dust opacity during the storm, with amplitudes exceeding 20 K in the southern hemisphere and 10 K in the northern hemisphere. The equatorially confined gravest Hough mode of the diurnal migrating tide is suppressed to undetectable levels and does not reemerge until after $L_s = 270°$.

Nearly all nonmigrating tides, including the diurnal Kelvin waves (DK1 and DK2), are repressed during the early portion of the storm's global extent at $L_s = 200°–210°$. The notable exception to this pattern being the diurnal westward propagating wavenumber 2 tide and possibly the diurnal westward propagating wavenumber 3 tide. This highlights the importance of the zonal distribution of aerosol forcing. Theoretical predictions and some previous work have shown that the wavenumber 1 diurnal Kelvin wave's temperature amplitude should remain relatively invariant to zonally uniform changing atmospheric dust loading [e.g., *Guzewich et al*., 2013b]. The changing pattern of dust lifting centers during the storm and the predominantly wavenumber 1 forcing by airborne dust invalidated that zonally uniform criterion. As a result of this wavenumber 1 dust forcing, the diurnal westward propagating wavenumber 2 tide, which appears in the $m = 1$ *T*-difference field in the satellite-relative perspective of TES, was strengthened. The amplitude of this tide increases to 4–8 K, with a similar amplification present in the MarsWRF dust storm simulation.

During the dust storm, dust at high altitude appeared to be tied to a slowly westward propagating wavenumber 1 wave [*Clancy et al*., 2010; *Guzewich et al*., 2013a]. This appears to have forced and/or maintained a strong ($>$10 K) wavenumber 1 northern hemisphere quasi-stationary (or slow-traveling) wave. The phase of this wave is consistent with its maximum located at the leading (western) edge of the high dust mixing ratios. At the same time, the wavenumber 2 stationary wave is rather weak in the northern hemisphere, contrary to typical conditions during this season of the year [*Guzewich et al*., 2012].

This study demonstrates the radical alteration by a global-scale dust storm to the wave forcing mechanisms normally present on Mars and provides a broader planet-wide view of the atmospheric dynamics during the storm. This adds confirmation to the coupling of waves between the tropics and higher latitudes (as described in *Wilson et al*. [2002]) through the link between the equatorial wave apparent in dust mixing ratio observations and associated inertial instability with the unusually strong high-latitude quasi-stationary wave. The demonstrated importance of the zonal structure in the dust mixing ratios confirms suggestions from previous studies that wave forcing in the atmosphere is more than a simplistic function of total atmospheric optical depth, which might be a more reasonable assumption if only the migrating tides were examined.

Acknowledgment
Guzewich was supported by a NASA Postdoctoral Program fellowship.

References

Banfield, D., B. Conrath, M. D. Smith, P. R. Christensen, and R. J. Wilson (2003), Forced waves in the Martian atmosphere from MGS TES nadir data, *Icarus*, *161*, 319–345, doi:10.1016/S0019-1035(02)00044-1.

Banfield, D. B., B. J. Conrath, P. J. Gierasch, R. John Wilson, and M. D. Smith (2004), Traveling waves in the Martian atmosphere from MGS TES nadir data, *Icarus*, *170*, 365–403.

Basu, S., J. Wilson, M. Richardson, and A. Ingersoll (2006), Simulation of spontaneous and variable global dust storms with the GFDL Mars GCM, *J. Geophys. Res.*, *111*, E09004, doi:10.1029/2005JE002660.

Bridger, A. F. C., and J. R. Murphy (1998), Mars' surface pressure tides and their behavior during global dust storms, *J. Geophys. Res.*, *103*, 8587–8601, doi:10.1029/98JE00242.

Cantor, B. A. (2007), MOC observations of the 2001 Mars planet-encircling dust storm, *Icarus*, *186*, 60–96, doi:10.1016/j.icarus.2006.08.019.

Chapman, S., and R. S. Lindzen (1970), *Atmospheric Tides*, D. Reidel, Norwell, Mass.

Clancy, R. T., B. J. Sandor, M. J. Wolff, P. R. Christensen, M. D. Smith, J. C. Pearl, B. J. Conrath, and R. J. Wilson (2000), An intercomparison of ground-based millimeter, MGS TES, and Viking atmospheric temperature measurements: Seasonal and interannual variability of temperatures and dust loading in the global Mars atmosphere, *J. Geophys. Res.*, *105*, 9553–9572.

Clancy, R. T., M. J. Wolff, B. A. Whitney, B. A. Cantor, M. D. Smith, and T. H. McConnochie (2010), Extension of atmospheric dust loading to high altitudes during the 2001 Mars dust storm: MGS TES limb observations, *Icarus*, *207*, 98–109.

Conrath, B. J. (1975), Thermal structure of the Martian atmosphere during the dissipation of the dust storm of 1971, *Icarus*, *24*, 36–46.

Forbes, J. M., and M. E. Hagan (2000), Diurnal Kelvin wave in the atmosphere of Mars:Towards an understandingof stationary density structures observed by the MGS Accelerometer, *Geophys. Res. Lett.*, *27*, 3563–3566.

Guzewich, S. D., E. R. Talaat, and D. W. Waugh (2012), Observations of planetary waves and nonmigrating tides by the Mars Climate Sounder, *J. Geophys. Res.*, *117*, E03010, doi:10.1029/2011JE003924.

Guzewich, S. D., E. R. Talaat, A. D. Toigo, D. W. Waugh, and T. H. McConnochie (2013a), High-altitude dust layers on Mars: Observations with the Thermal Emission Spectrometer, *J. Geophys. Res. Planets*, *118*, 1177–1194, doi:10.1002/jgre.20076.

Guzewich, S. D., A. D. Toigo, M. I. Richardson, C. E. Newman, E. R. Talaat, D. W. Waugh, and T. H. McConnochie (2013b), The impact of a realistic vertical dust distribution on the simulation of the Martian General Circulation, *J. Geophys. Res. Planets*, *118*, 980–993, doi:10.1002/jgre.20084.

Haberle, R. M., C. B. Leovy, and J. M. Pollack (1982), Some effects of global dust storms on the atmospheric circulation of Mars, *Icarus*, *50*, 322–367, doi:10.1016/0019-1035(82)90129-4.

Hinson, D., G. Tyler, J. Hollingsworth, and R. Wilson (2001), Radio occultation measurements of forced atmospheric waves on Mars, *J. Geophys. Res.*, *106*, 1463–1480, doi:10.1029/2000JE001291.

Kahn, R. A., T. Z. Martin, R. W. Zurek, and S. W. Lee (1992), The Martian dust cycle, in *Mars*, edited by H. H. Kieffer et al., pp. 1017–1053, University of Arizona Press, Tucson, Ariz.

Lee, C., et al. (2009), Thermal tides in the Martian middle atmosphere as seen by the Mars Climate Sounder, *J. Geophys. Res.*, *114*, E03005, doi:10.1029/2008JE003285.

Leovy, C. B., and R. W. Zurek (1979), Thermal tides and Martian dust storms: Direct evidence for coupling, *J. Geophys. Res.*, *84*, 2956–2968, doi:10.1029/JB084iB06p02956.

Leovy, C. B. (1981), Observations of Martian tides over two annual cycles, *J. Atmos. Sci.*, *38*, 30–39, doi:10.1175/1520-0469(1981)038<0030:OOMTOT>2.0.CO;2.

Lewis, S. R., and P. R. Barker (2005), Atmospheric tides in a Mars general circulation model with data assimilation, *Adv. Space Res.*, *36*, 2162–2168, doi:10.1016/j.asr.2005.05.122.

Liu, J., M. I. Richardson, and R. J. Wilson (2003), An assessment of the global, seasonal, and interannual spacecraft record of Martian climate in the thermal infrared, *J. Geophys. Res.*, *108*(E8), 5089, doi:10.1029/2002JE001921.

Martinez-Alvarado, O., L. Montabone, S. R. Lewis, I. M. Moroz, and P. L. Read (2009), Transient teleconnection event at the onset of a planet-encircling dust storm on Mars, *Ann. Geophys.*, *27*, 3663–3676.

McConnochie, T. H., and M. D. Smith (2011), Correcting Mars Global Surveyor Thermal Emission Spectrometer (MGS-TES) high altitude (40–65 km) temperature retrievals for instrumental correlated noise and biases, Abstract #P21A-1639 presented at 2011 Fall Meeting, AGU, San Francisco, Calif.

Montabone, L., S. R. Lewis, P. L. Read, and D. P. Hinson (2006), Validation of Martian meteorological data assimilation for MGS/TES using radio occultation measurements, *Icarus*, *185*, 113–132, doi:10.1016/j.icarus.2006.07.012.

Montabone, L., O. Martinez-Alvarado, S. R. Lewis, P. L. Read, and R. J. Wilson (2008), Teleconnection in the Martian atmosphere during the 2001 planet-encircling dust storm, Abstract 9077, Mars Atmosphere: Modeling and Observations Workshop, Williamsburg, Va.

Montmessin, F., F. Forget, P. Rannou, M. Cabane, and R. M. Haberle (2004), Origin and role of water ice clouds in the Martian water cycle as inferred from a general circulation model, *J. Geophys. Res.*, *109*, E10004, doi:10.1029/2004JE002284.

Moudden, Y., and J. M. Forbes (2011a), Simulated planetary wave-tide interactions in the atmosphere of Mars, *J. Geophys. Res.*, *116*(E1), E01004, doi:10.1029/2010JE003698.

Moudden, Y., and J. M. Forbes (2011b), First detection of wave interactions in the middle atmosphere of Mars, *Geophys. Res. Lett.*, *38*, L04202, doi:10.1029/2010GL045592.

Richardson, M. I., A. D. Toigo, and C. E. Newman (2007), PlanetWRF: A general purpose, local to global numerical model for planetary atmospheric and climate dynamics, *J. Geophys. Res.*, *112*, E09001, doi:10.1029/2006JE002825.

Salby, M. L., P. F. Callaghan (2001), Seasonal amplification of the 2-day wave: Relationship between normal mode and instability, *J. Atmos. Sci.*, *58*, 1858–1869, doi:10.1175/1520-0469(2001)058<1858:SAOTDW>2.0.CO;2.

Smith, M. D., J. C. Pearl, B. J. Conrath, and P. R. Christensen (2001), Thermal Emission Spectrometer results: Mars atmospheric thermal structure and aerosol distribution, *J. Geophys. Res.*, *106*, 23,929–23,945, doi:10.1029/2000JE001321.

Smith, M. D., J. C. Pearl, B. J. Conrath, and P. R. Christensen (2002), Thermal Emission Spectrometer observations of a planet-encircling dust storm, *Icarus*, *157*, 250–263.

Smith, M. D. (2004), Interannual variability in TES atmospheric observations of Mars during 1999–2003, *Icarus*, *167*, 148–165.

Smith, M. D. (2008), Spacecraft observations of the Martian atmosphere, *Ann. Rev. Earth Planet. Sci.*, *36*, 191–219.

Strausberg, M. J., H. Wang, M. I. Richardson, S. P. Ewald, and A. D. Toigo (2005), Observations of the initiation and evolution of the 2001 Mars global dust storm, *J. Geophys. Res.*, *110*, E02006, doi:10.1029/2004JE002361.

Toigo, A., C. Lee, C. E. Newman, and M. I. Richardson (2012), The impact of resolution on the dynamics of the Martian global atmosphere: Varying resolution studies with the MarsWRF GCM, *Icarus*, *221*(1), 276–288, doi:10.1016/j.icarus/2012.07.020.

Wang, H., M. I. Richardson, R. J. Wilson, A. P. Ingersoll, and A. D. Toigo (2003), Cyclones, tides, and the origin of cross-equatorial dust storms on Mars, *Geophys. Res. Lett.*, *30*(9), 1488, doi:10.1029/2002GL016828.

Wilson, R. J., and K. Hamilton (1996), Comprehensive model simulation of thermal tides in the Martian atmosphere, *J. Atmos. Sci.*, *53*, 1290–1326, doi:10.1175/1520-0469(1996)053<1290:CMSOTT>2.0.CO;2.

Wilson, R. J. (2000), Evidence for diurnal period Kelvin waves in the Martian atmosphere from Mars Global Surveyor TES data, *Geophys. Res. Lett.*, *27*, 3889–3892, doi:10.1029/2000GL012028.

Wilson, R. J., and M. I. Richardson (2000), The Martian atmosphere during the Viking Mission, I: Infrared measurements of atmospheric temperatures revisited, *Icarus*, *145*(2), 555–579, doi:10.1006/icar.2000.6378.

Wilson, R. J. (2002), Evidence for nonmigrating thermal tides in the Mars upper atmosphere from the Mars Global Surveyor Accelerometer experiment, *Geophys. Res. Lett.*, *29*(7), 1120, doi:10.1029/2001GL013975.

Wilson, R. J., D. Banfield, B. J. Conrath, and M. D. Smith (2002), Traveling waves in the northern hemisphere of Mars, *Icarus*, *29*(14), doi:10.1029/2002GL014866.

Wilson, R. J., S. R. Lewis, L. Montabone, and M. D. Smith (2008a), Influence of water ice clouds on Martian tropical atmospheric temperatures, *Geophys. Res. Lett.*, *35*, L07202, doi:10.1029/2007GL032405.

Wilson R. J., S. R. Lewis, and L. Montabone (2008b), Thermal tides in an assimilation of three years of Thermal Emission Spectrometer data from Mars Global Surveyor, Abstract 9022, Mars Atmosphere: Modeling and Observations Workshop, Williamsburg, Va.

Withers, P., R. Pratt, J.-L. Bertaux, and F. Montmession (2011), Observations of thermal tides in the middle atmosphere of Mars by the SPICAM instrument, *J. Geophys. Res.*, *116*, E11005, doi:10.1029/2011JE003847.

Wolff, M. J., et al. (2006), Constraints on dust aerosols from the Mars Exploration Rovers using MGS overflights and Mini-TES, *J. Geophys. Res.*, *111*, E12S17, doi:10.1029/2006JE002786.

Zurek, R., and C. B. Leovy (1981), Thermal tides in the dusty Martian atmosphere: A verification of theory, *Science*, *213*, 437–439, doi:10.1126/science.213.4506.437.

Zurek, R. (1988), Free and forced modes in the Martian atmosphere, *J. Geophys. Res.*, *93*, 9452–9462, doi:10.1029/JD093iD08p09452.